The Astrophysical Journal, 832:186 (15pp), 2016 December 1 doi:10.3847/0004-637X/832/2/186

MAGNETICALLY DOMINATED PARALLEL INTERSTELLAR FILAMENTS IN THE INFRARED DARK CLOUD G14.225-0.506*

Fábio P. Santos[1], Gemma Busquet[2], Gabriel A. P. Franco[3], Josep Miquel Girart[2,4], and Qizhou Zhang[4]
[1] Department of Physics and Astronomy, Northwestern University, 2145 Sheridan Road, Evanston, IL 60208, USA; fabiops@northwestern.edu
[2] Institut de Ciències de l'Espai (CSIC-IEEC), Campus UAB, Carrer de Can Magrans, S/N E-08193 Bellaterra, Catalunya, Spain; busquet@ice.cat, girart@ice.cat
[3] Departamento de Física—ICEx—UFMG, Caixa Postal 702, 30.123-970 Belo Horizonte, MG, Brazil; franco@fisica.ufmg.br
[4] Harvard-Smithsonian Center for Astrophysics, 60, Garden Street, Cambridge, MA 02138, USA; qzhang@cfa.harvard.edu
Received 2016 February 16; revised 2016 September 23; accepted 2016 September 25; published 2016 November 30

ABSTRACT

The infrared dark cloud G14.225-0.506 (IRDC G14.2) displays a remarkable complex of parallel dense molecular filaments projected on the plane of the sky. Previous studies of dust emission and molecular lines have speculated whether magnetic fields could have played an important role in the formation of such elongated structures, which are hosts to numerous young stellar sources. In this work we have conducted a vast polarimetric survey at optical and near-infrared wavelengths in order to study the morphology of magnetic field lines in IRDC G14.2 through the observation of background stars. The orientation of interstellar polarization, which traces magnetic field lines, is perpendicular to most of the filamentary features within the cloud. Additionally, the larger-scale molecular cloud as a whole exhibits an elongated shape also perpendicular to magnetic fields. Estimates of magnetic field strengths indicate values in the range 320–550 μG, which allow sub-alfvénic conditions, but do not prevent the gravitational collapse of hub–filament structures, which in general are close to the critical state. These characteristics suggest that magnetic fields played the main role in regulating the collapse from large to small scales, leading to the formation of series of parallel elongated structures. The morphology is also consistent with numerical simulations that show how gravitational instabilities develop when subjected to strong magnetic fields. Finally, the results corroborate the hypothesis that strong support from internal magnetic fields might explain why the cloud seems to be contracting on a timescale 2–3 times longer than what is expected from a free-fall collapse.

Key words: dust, extinction – evolution – ISM: individual objects (SDC G14.225-0.506) – ISM: magnetic fields – stars: formation – techniques: polarimetric

1. INTRODUCTION

Filamentary structures in the interstellar medium (ISM) are commonly observed in many different types of environments, such as diffuse nearby clouds (Penprase et al. 1998; McClure-Griffiths et al. 2006), giant molecular clouds (Lis et al. 1998; Hill et al. 2011), H II regions (Anderson et al. 2012; Minier et al. 2013), and supernova remnants (Gomez et al. 2012). Their presence in the Milky Way Galaxy has typically been revealed by numerous different observing techniques, including visual extinction, H I emission, molecular-line surveys, and thermal emission from dust. In particular, dense molecular filaments are in general associated with star-forming regions. Myers (2009) pointed out, for instance, that all the nearest low-mass star formation sites (within 300 pc from the Sun) seem to present a hub–filament structure, with some of them showing evenly spaced parallel filaments.

Although filaments have been known for many decades, observations of thermal emission from dust made by the *Herschel* space observatory in more recent years (Pilbratt et al. 2010) have provided a groundbreaking understanding of filaments in the ISM, showing that they are in fact ubiquitous, especially within giant molecular clouds (André et al. 2010; Molinari et al. 2010), which include both quiescent and star-forming regions. The recognition of filaments as active sites of star formation was made clear by the fact that most of the observed pre-stellar cores seem to form in gravitationally unstable filaments (André et al. 2010; Arzoumanian et al. 2011). That led to an increasing interest in explaining how these structures are formed and how they evolve. Although turbulent motions in the ISM might be responsible for the formation of some filaments (Arzoumanian et al. 2011), other plausible explanations are the convergence of flows, large-scale collisions between filaments, and gravitational instabilities (Nakajima & Hanawa 1996; Jiménez-Serra et al. 2010; Schneider et al. 2010; Nakamura et al. 2012; Van Loo et al. 2014); the last scenario is also supported by numerical models (Gómez & Vázquez-Semadeni 2014).

In addition, it is well known that the ISM is entirely threaded by a large-scale structure of magnetic field lines that pervades the whole Galaxy (Mathewson & Ford 1970; Reiz & Franco 1998; Heiles 2000; Santos et al. 2011). This includes the filaments as well as the dense molecular cores where star formation is taking place (e.g., Girart et al. 2006, 2009; Alves et al. 2008; Zhang et al. 2014; Li et al. 2015). In general, a small level of ionization is sufficient to provide enough coupling between the magnetic fields and the interstellar gas (Heiles & Crutcher 2005). Indeed, magnetic fields might also play an important role in generating filamentary structures, as suggested by several authors (Nagai et al. 1998; Nakamura & Li 2008; Li et al. 2013, 2015).

G14.225-0.506 (hereafter IRDC G14.2) is an infrared dark cloud at a distance of $1.98^{+0.13}_{-0.12}$ kpc (Xu et al. 2011; Wu et al. 2014) that shows an intricate pattern of filaments. These filaments are clearly seen in absorption against the bright mid-infrared background Galactic emission, as identified by Peretto

* Based on observations collected at Observatório do Pico dos Dias, operated by Laboratório Nacional de Astrofísica (LNA/MCT, Brazil).

& Fuller (2009) using *Spitzer Space Telescope* data.[5] This region is part of a larger complex of clouds including the well-known star-forming area M17 (Elmegreen & Lada 1976). Other studies revealed signs of star formation such as H_2O maser emission (Jaffe et al. 1981; Palagi et al. 1993; Wang et al. 2006) and emission from dense gas tracers toward IRAS 18153-1651, which is one of the bright infrared sources in the region (Plume et al. 1992; Anglada et al. 1996), with a luminosity of $1.1 \times 10^4\ L_\odot$. Furthermore, many young stellar objects were later identified by Povich & Whitney (2010, who labeled this region as M17 SWex), including several Class 0 and I sources. Although IRDC G14.2 does not appear to host very massive stars, a few ultra-compact H II regions are located among its filamentary structures (Jaffe et al. 1982; Bronfman et al. 1996). Busquet et al. (2013, herafter Paper I) presented ammonia observations in IRDC G14.2, inferring that the parallel arrangement of most filaments could be explained by the gravitational collapse of an unstable thin layer threaded by magnetic fields (Van Loo et al. 2014).

The sky-projected morphology of magnetic field lines may be mapped through studies of the interstellar polarization due to magnetically aligned dust particles, either through observations of background starlight or via direct thermal emission from dust. Although the detailed aspects of the alignment mechanism is one of the most long-standing issues in the physics of the ISM, it is now generally believed that radiative torques are a dominant effect (Dolginov & Silantev 1976; Draine & Weingartner 1996; Lazarian 2007), as suggested by different studies (Whittet et al. 2008; Andersson et al. 2011; Alves et al. 2014; Jones et al. 2015). Even though different large-scale surveys of polarized emission have been providing an unprecedented view of magnetic fields in the ISM (such as *Planck*—Planck Collaboration et al. 2015—and BLASTPol—Fissel et al. 2016), the spatial resolution needed to distinguish filamentary features in distant clouds is still a challenge, making optical and near-infrared (NIR) polarimetry of background starlight a viable option.

IRDC G14.2 is an ideal target for investigating the role of magnetic fields in generating filamentary structures. In this work, we present a vast extension of a preliminary polarimetric data set previously shown in Paper I. This includes optical and NIR observations encompassing the whole filamentary network of IRDC G14.2, as well as the associated large-scale molecular cloud. In Section 2 we describe the polarimetric observations, as well as the data processing. Results and analysis are shown in Section 3, which includes studies of the relative orientation between magnetic fields and the cloud and internal filaments, as well as estimates of various important physical paramenters. A detailed discussion of the results is given in Section 4 and the final conclusions are summarized in Section 5.

2. OBSERVATIONAL DATA

The polarization data used in this work were collected at the 1.6 m telescope of the Pico dos Dias Observatory (OPD,[6] Brazil), in a series of observations during 2011 July, 2013 May, and 2014 April. A small portion of the NIR data, focused on a fraction of the filamentary complex IRDC G14.2, was previously shown in its preliminary version in Paper I. The current work presents a widely extended version of the same NIR data set, covering the entire group of interstellar filaments (in the *H* band). Additionally, an optical survey was conducted (using the *R* band), to map an even larger area comprising the large-scale cloud in which the dense filaments are embedded.

The instrumental set was composed of the IAGPOL polarimeter, together with an imaging detector, which could be either an optical CCD or an NIR detector (HAWAII 1024×1024 pixels—CamIV), depending on the spectral ranges used in each observing run. The polarimeter consists of a rotating achromatic half-wave plate followed by an analyzer and a spectral band filter (for more information on the instrument and the data reduction process, see Magalhaes et al. 1996; Santos et al. 2012). By rotating the half-wave plate in discrete and successive angles of $\psi = 22.^\circ5$, the orientation of linear polarization of the incident light changes in steps of 45°. The analyzer splits the light beam into two orthogonally polarized components, which are simultaneously collected by the detector. Consecutive rotations of the half-wave plate produce relative intensity variations between the two components, defining an oscillating modulation function proportional to $\cos 4\psi_i$. The flux-normalized Stokes parameters Q and U are determined through a least-squares fitting of this function, using the relative intensity for all targets at each position of the half-wave plate. Thereafter, this allows calculation of the degree of polarization (p) and the orientation in the plane of the sky (θ).

In this way, p and θ are found for the majority of the point-like sources detected in each observing field. The optical field of view covers an area of $11' \times 11'$ as opposed to $4' \times 4'$ for the NIR detector. Therefore, a mosaic-mapping was adopted to cover a wider area of the sky. For IRDC G14.2, the *R*-band observations consisted of a 5×5 mosaic grid (25 fields), resulting in a mapping of an area of $\sim 53' \times 53'$. The *H*-band observations consisted of eight fields, and were focused on the filamentary structures located approximately at the center of the larger-scale area covered by the *R*-band survey. For each optical field, two sets of eight positions of the half-wave plate were used, with a long (60 s) and a short (10 s) exposure at each position. For the NIR, 60 images of 10 s each were acquired for each position of the half-wave plate, while dithering the telescope to remove the thermal background signal, adding up to a total exposure of 600 s per position (the same procedure was repeated in each field of view).

Image processing and photometry were performed using IRAF[7] routines (Tody 1986), which typically consist of a correction of the bias and flat-field pattern, background sky subtraction, detection of point-like sources (with a threshold of 5σ above the local background), flux measurements, and configuration of the image's astrometry (world coordinate system). Computation of linear polarization for each star was done with the PCCDPACK set of routines (Pereyra 2000), and calibration of the zero-point polarization angle was based on polarimetric standard sources observed each night (Wilking et al. 1980, 1982; Clemens & Tapia 1990; Turnshek et al. 1990; Larson et al. 1996). Finally, de-biased polarization

[5] Based on the Galactic Legacy Infrared Mid-Plane Survey Extraordinaire (GLIMPSE, Benjamin et al. 2003) and the Multiband Imaging Photometer for Spitzer Galactic Plane Survey (MIPSGAL, Carey et al. 2009).

[6] The Pico dos Dias Observatory is operated by the Brazilian National Laboratory for Astrophysics (LNA), a research institute of the Ministry of Science, Technology and Innovation (MCTI).

[7] IRAF is distributed by the National Optical Astronomy Observatories, which are operated by the Association of Universities for Research in Astronomy, Inc., under cooperative agreement with the National Science Foundation.

values were computed ($p \rightarrow (p^2 - \sigma_p^2)^{1/2}$, Wardle & Kronberg 1974). In the analysis that follows, we use only detections with values of p/σ_p greater than 4 and 5 for the *R*- and *H*-band samples, respectively.

3. RESULTS AND ANALYSIS

3.1. Polarization Maps and General Interstellar Features

Orientations of polarization detections are assumed to trace the sky-projected orientation of magnetic field lines. To understand their relation to the surrounding ISM, we begin by plotting segments over different images covering distinct spectral ranges. Figures 1(a) and (b) respectively show the entire ensembles of *R*-band (red) and *H*-band (blue) polarization data. The sizes of the segments are proportional to $\sqrt{p}$, allowing a less biased visualization of the magnetic field morphology, particularly in this case where there is a mixture of segments displaying large variations in the degree of polarization.

In this work, the analyses of the *R*-band and *H*-band polarimetric samples are distinguished by the fact that they are useful in tracing respectively the large-scale and the small-scale magnetic field structure around IRDC G14.2. More specifically, here we define small scales as the typical range of lengths of the filaments found in IRDC G14.2 (~1–3 pc, green NH_3 contours in Figure 1(b)), and large scales as sizes of the order of the molecular cloud in which the filaments are embedded (~20–40 pc, cyan visual extinction contours—A_V—in Figure 1(a)). On one hand, while the *R*-band detections are limited by extinction to trace only more diffuse ISM, they are distributed over a large area covering the molecular cloud's surroundings. On the other hand, the *H*-band polarimetry covers only the central areas, but is less affected by extinction and therefore a large number of segments are concentrated around the filaments.

In both Figures 1(a) and (b) the background image corresponds to Hα observations (Parker et al. 2005). Thus, the image shows both stellar point sources and patches of bright extended emission due to the presence of the H II region RCW 157, also known as Sh 2–44 (outlined by the curved yellow dashed line). The association of the H II region RCW 157 with IRDC G14.2 is not clear because there is a discrepancy in the distance of the former (~2 kpc according to Avedisova & Palous (1989), and 3.7 kpc according to Deharveng et al. (2010) and Lockman (1989)). In any case, in this work we excluded from the analysis the polarization data around the region RCW 157 since the original morphology of magnetic field lines might have been distorted by the expansion of the ionized volume. More discussion will be given in Section 4.4.

Figures 1(c) and (d) show the foreground-corrected polarization segments, in respectively the *R* and *H* bands. The detailed process of foreground correction is discussed in Section 3.2. Background images in this case correspond to *Herschel*-SPIRE 250 μm (Figure 1(c)) and *Spitzer* 8 μm (Figure 1(d)). The large-scale dust cloud and the complex of filamentary structures embedded within it are clearly observed in these images. The close-up view from *Spitzer* (Figure 1(d)) is a higher-resolution view of the intricate pattern of interstellar filaments, seen in absorption against the Galactic background infrared radiation.

3.2. Visual Extinction Estimates and Foreground Polarization Correction

Considering the distance to IRDC G14.2, it is likely that a considerable fraction of the detections actually correspond to foreground stars (particularly those detected in the *R*-band mapping). Therefore, two distinct operations must be applied to correct for the foreground contamination:

1. Correction A: foreground stars must be identified at least statistically, and removed from the sample;
2. Correction B: the polarization component produced by the foreground material must be determined and subtracted from the background sources.

In the general direction of the dark cloud, stars distributed at different distances probe interstellar polarization features produced by different interstellar components. Since individual distances are not known, one may use the visual extinction as a general proxy, giving us an approximate idea of the star's location along the line of sight.

Estimates of the visual extinction A_V for each stellar object were obtained based on 2MASS photometric data (Skrutskie et al. 2006). Among the total of 4627 and 584 stars from our *R*-band and *H*-band samples, respectively, 1227 and 337 were either not found in the 2MASS catalog or excluded due to poor photometry in at least one of the NIR bands (*J*, *H*, or *Ks*). Thus, the following analysis applies only to the objects found in the 2MASS catalog with valid photometric values.

The method of determining visual extinction is based on color–color diagrams $(J - H) \times (H - Ks)$, which are shown in Figures 2(a) and (b) for the *R*-band and *H*-band polarimetric samples, respectively. As may be noted, reddening causes points to spread along a band (gray dashed lines), since each data point is displaced from its de-reddened position an amount proportional to the visual extinction. Therefore, by de-reddening each point upon reaching the locus of the main sequence, it is possible to estimate A_V by applying general interstellar relations given by Fitzpatrick (1999). This method is not meant to provide a highly precise determination of A_V, since individual spectral types are not known and general assumptions regarding the relation between color excess and extinction have to be made (Fitzpatrick 1999). However, it is sufficiently robust to provide an approximate estimate, as needed in this work. It is important to point out that when de-reddening each point along the reddening band, the locus of the main sequence can be crossed twice (early-type and later-type stars), suggesting that there is an apparent degeneracy in the A_V estimate. However, assuming the limits of 2MASS photometric completeness, it is easy to show that unreddened main-sequence stars with spectral types later than G5 (the yellow line starting on the yellow plus sign) are too faint to be observed at such distances. Thus, the late-type portion of the main sequence can be ignored (the yellow line) and only the early-type locus of the main sequence is used, removing the ambiguity. Also notice that the early-type portion of this locus is superposed on the locus of giants and supergiants in a $(J - H) \times (H - Ks)$ diagram, and thus the A_V estimate does not depend on the luminosity class. For the *R* band, only objects inside the reddening band are considered valid for this calculation (red or blue crosses), while objects outside (black dots) are excluded. In this way, sources with infrared color excess (typically displaced to the right side of the reddening band), which are known to present circumstellar disks (and

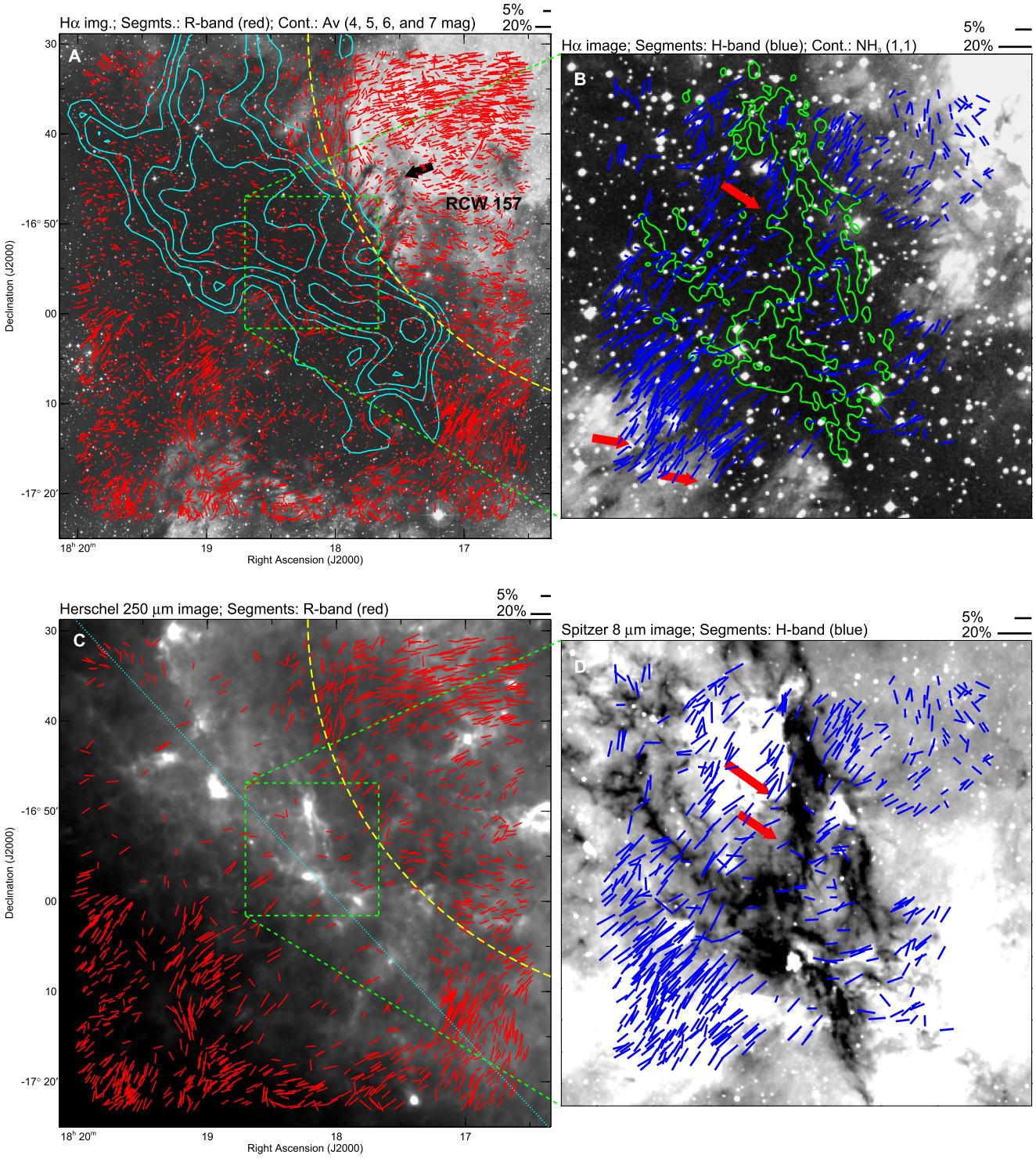

Figure 1. Polarization maps of IRDC G14.2 showing the entire data sets in the *R* band (a) and *H* band (b), as well as the foreground-corrected samples (see Section 3.2) in the *R* band (c) and *H* band (d). The optical mapping (red segments) covers a large area around the cloud that is indicated by the cyan-colored A_V contours in panel (a) (4, 5, 6 and 7 mag levels, Dobashi et al. 2013). The NIR data set (blue segments) is focused on the central filamentary features (green contours in panel (b), representing the integrated $NH_3(1, 1)$ emission with levels of 40 mJy beam^{-1} km s^{-1}, from Paper I). The lengths of polarization segments are scaled proportional to $\sqrt{p}$ (each panel shows reference sizes for 5% and 20% segments in the top right). Background images are from the SuperCOSMOS Hα survey in panels (a) and (b) (Parker et al. 2005), from *Herschel*-SPIRE 250 μm in panel (c) and from *Spitzer*-IRAC 8 μm in panel (d). The different wavelengths reveal emission features from different ISM components, such as ionized gas, cold or warm dust. The area of RCW 157 is indicated by the yellow dashed line in panels (a) and (c). Pillars at the edge of this area are located by the black arrow (see Section 4.4). Red arrows indicate striations perpendicular to the filaments, in both the Hα image (b) and the *Spitzer* image ((d), see Section 4.1). The large-scale orientation of the cloud is indicated by the dotted cyan line in panel (c) (≈43° relative to the north celestial pole).

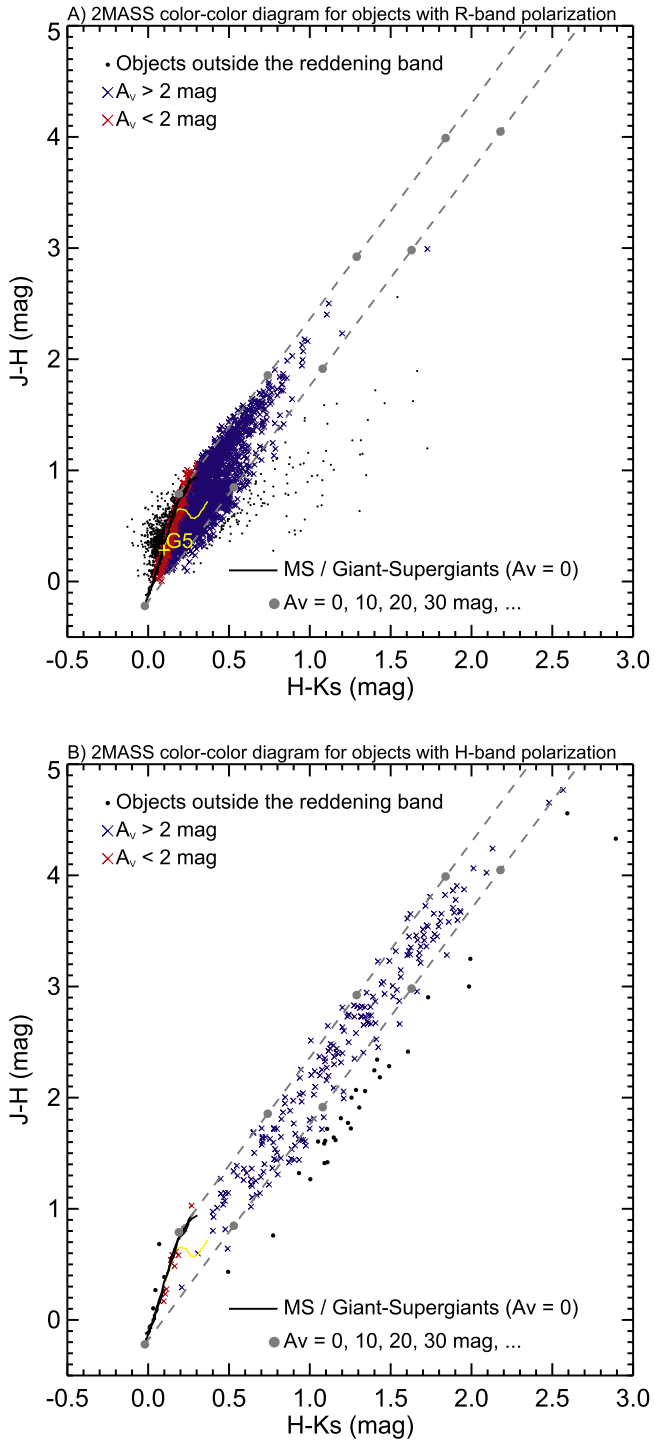

Figure 2. Color–color $(J-H)\times(H-Ks)$ diagrams based on 2MASS for objects from the *R*-band (a) and *H*-band (b) data sets. The locus that corresponds to the unreddened ($A_V=0$) main sequence, giants, and supergiants is indicated by a solid line (Koornneef 1983; Carpenter 2001). The reddening band (parallel to the reddening vector, Fitzpatrick 1999) is represented by dashed gray lines, in which each bullet indicates an increment of 10 mag. The yellow line represents main-sequence stars with spectral types later than G5.

therefore possibly intrinsic polarization by scattering), are automatically removed.

The *R*-band diagram shows that there are stars with a distribution of various extinction levels. Analyzing maps of $E(b–y)$ reddening from Reis et al. (2011), we notice that along the line of sight to the cloud, the foreground ISM closer to the Sun ($d \lesssim 300$ pc) contributes $A_V \sim 1$ mag (assuming the general relation $A_V = 4.3E(b–y)$). Estimates of the extinction and polarization levels associated with the material beyond these local regions may be made by studying the compilation of P_V data (degree of polarization in the *V* band) and $E(B-V)$ data (interstellar reddening) by Heiles (2000) as a function of distance. Considering a radius of 1° centered on the cloud, 15 stars with distance less than 2.0 kpc are found. Their mean *R*-band degree of polarization and angle are respectively $(0.7 \pm 0.2)\%$ and 67°, giving us an initial idea of the level of foreground polarization. It is important to point out that we have converted the degree of polarization from *V* to *R* band using the relation by Serkowski et al. (1975), assuming typical grain sizes, which corresponds to a peak in the polarization spectrum around $\lambda_{\max} = 0.55$ μm. The mean $E(B-V)$ value using the same 15 objects from Heiles (2000) is 0.6 mag, corresponding to $A_V \approx 2.0$ mag (assuming $A_V = 3.1E(B-V)$).

Using the 2 mag level as a general proxy for the foreground visual extinction, we proceed with the analysis by constructing the histograms in Figure 3. The first histogram (Figure 3(a)) shows the distribution of polarization values for stars with $A_V < 2$ mag, while Figure 3(b) shows the distribution for $A_V > 2$ mag. A peak is seen in the first case (the blue Gaussian fit), while for higher extinctions (Figure 3(b)) the Gaussian profile vanishes, shifting to a rather flat distribution. This indicates that objects encompassed by the Gaussian curve are probably foreground objects, while sources with higher extinction are most likely background stars. To determine the foreground polarization angle, the third histogram (Figure 3(c)) shows θ_R for stars with $A_V < 2$ mag and $p < 1.5\%$ (i.e., considering only objects below the Gaussian curve of Figure 3(a)). From the peak of the Gaussian fits of Figures 3(a) and (c), we estimate values of respectively 0.67% and 64° for polarization percentage and orientation angle in the *R* band, matching very well the expectations based solely on the data of Heiles (2000). Additionally, the foreground value obtained is practically invariant under slight changes in the A_V and *p* cutoffs used here, showing that this is a robust computation.

Notice that the shape of the distribution of polarization angle in Figure 3(c) deviates slightly from a Gaussian, suggesting that the foreground component is not perfectly uniform across the field. This is not unexpected, given the wide field of view of the *R*-band survey area. The non-uniformity probably corresponds to a smooth change in the foreground polarization angle across the field, since the distribution shows a unique asymmetric wide peak instead of clearly distinguishable multiple peaks. Even though in this work we are adopting a single average foreground component, it is relevant to point out that for the purposes of the removal of this component from background sources (Correction B), the analysis that will be presented in Section 3.3 is very robust, and the same results are obtained even if no subtraction is applied (although Correction A is still important). The main reason is that the foreground component is usually small compared with the polarization levels of background stars, for which the molecular cloud component is predominant.

To apply Correction A, in order to be conservative in the selection of background sources, we consider only those with $A_V > 2$ mag and $p > 2.0\%$ (i.e., those outside the range of the

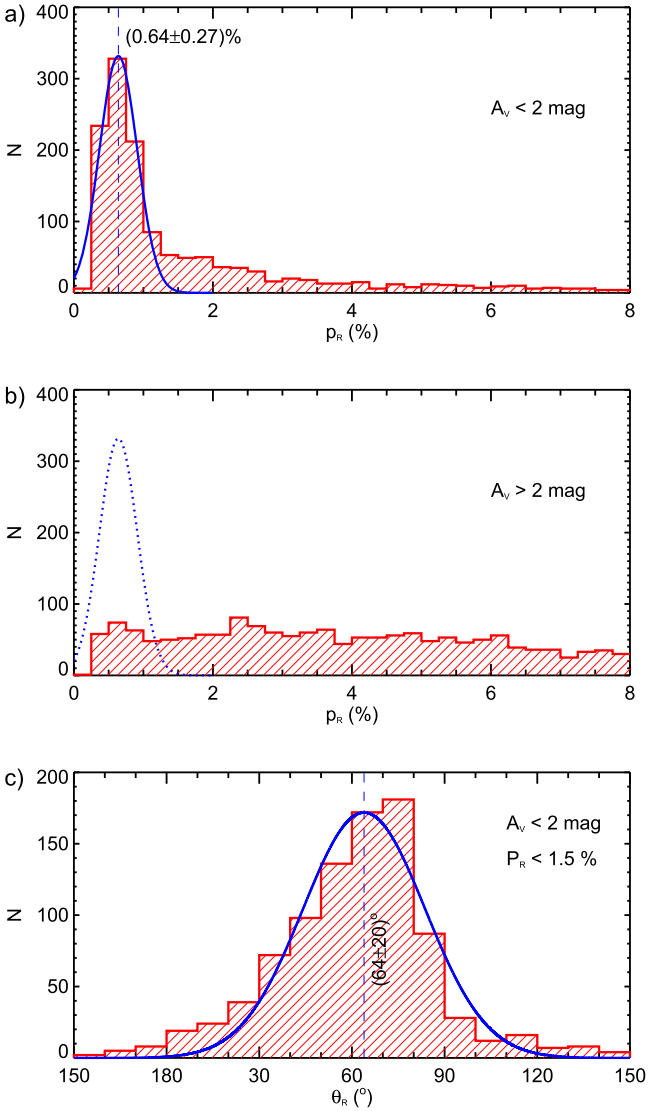

Figure 3. Histograms used to estimate the foreground contribution to the *R*-band polarimetric sample: (a) the distribution of p_R for $A_V < 2$ mag (which is a general proxy for the foreground extinction), with a Gaussian fit peaked at 0.64%; (b) the distribution for $A_V > 2$ mag (the Gaussian fit from (a) is shown for reference); (c) the distribution of θ_R, considering only polarization detections with $A_V < 2$ mag and $p_R < 1.5\%$. The Gaussian fit indicates an average foreground orientation of polarization of ≈64°.

Gaussian fit from Figure 3(a)), and we also exclude sources not found in 2MASS or rejected due to poor photometry. For Correction B, we first calculate the mean foreground Stokes parameters Q and U using the mean foreground polarization that was obtained previously ($p_V = 0.67\%$ and $\theta_V = 64°$). Then, we subtract these mean values of foreground Q and U from each background star, finally determining a sample of foreground-corrected *R*-band detections that are probably mostly composed of background sources. The polarization segment for the foreground-corrected sample is shown in Figure 1(c).

In the case of the *H*-band sample, the color–color diagram (Figure 2(b)) shows that only a few stars are low-extinction sources ($A_V < 2$ mag). These few objects are excluded from the final sample, yielding the map in Figure 1(d), in which most sources are probably from the background, given their A_V levels. The small fraction of foreground stars found in the *H*-band data set with 2MASS data suggests that, even considering the entire data set (including objects not found in 2MASS or excluded due to poor photometry), the vast majority of stars are probably background sources. Thus, we consider objects not found in 2MASS (or rejected) to be background sources for the *H*-band polarization analysis in this work. When subtracting the foreground component from background sources (Correction B), we find that the contribution is negligible in the *H* band: if $p = 0.67\%$ in the *R* band, then assuming the Serkowski relation, the *H*-band foreground polarization would be approximately 0.15%. Since this is a small level of polarization, lower than the typical uncertainty in the degree of polarization, we choose to ignore its contribution. This avoids introducing unnecessary systematic uncertainties, since the estimate of 0.15% for the *H*-band foreground polarization (extrapolating from the *R* band) involves assumptions regarding the peak of the spectral function of the polarization.

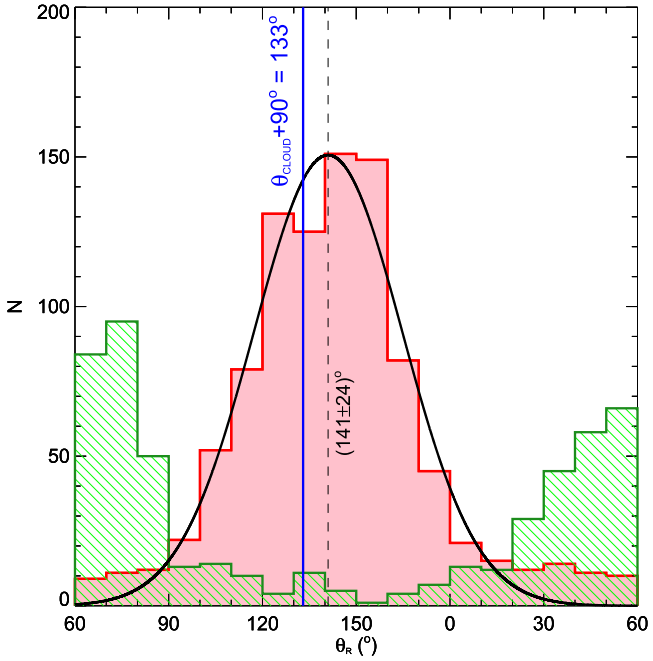

Figure 4. Histogram (red) of the foreground-corrected orientation of polarization segments in the *R* band (as shown in Figure 1(c)), excluding the region of RCW 157. The peak of the distribution (≈141°) is found through the Gaussian fit, and is approximately perpendicular to the large-scale orientation of the cloud ($\theta_{cloud} + 90° = 133°$). The green histogram corresponds to foreground objects removed from the sample (see Correction A in Section 3.2).

3.3. Relation between Polarization Segments and the Large-scale Orientation of the Cloud

After removal of the foreground stars from the *R*-band sample, it is possible to investigate the relation between the orientation of polarization segments and the large-scale cloud in which the interstellar filaments are embedded. This may help to determine the range of spatial scales on which magnetic fields might be important in regulating the gravitational collapse.

Figure 4 shows a histogram of *R*-band polarization angles (red), excluding the area defined by the H II region RCW 157 (above the dashed yellow line in Figure 1(a)). Although there is a large dispersion, a peak around 141° is clearly identified (as shown by the Gaussian fit). In comparison, the direction perpendicular to the cloud ($\theta_{cloud} + 90°$) is indicated by the

blue line as ∼133° (the cloud's direction, ≈43°, is shown by the cyan-colored dotted line in Figure 1(c)). It is clear that there is an overall correlation between the large-scale magnetic field lines and the direction perpendicular to the cloud.

It is important to point out that, particularly for this analysis, the prior removal of foreground sources was essential (Correction A), since these comprised a considerable fraction of the vector sample. The green histogram in Figure 4 shows foreground stars that were removed from the sample. Notice that foreground segments in general are parallel to the cloud, which is opposite to the trend for background sources. Comparing Figures 1(a) and (c), it is straightforward to visualize the sample of foreground stars that has been removed (which are mostly low polarization detections parallel to the orientation of the cloud). Therefore, if not removed first, this component would have introduced considerable contamination in this analysis, impairing the notion that on-site magnetic field lines in general are perpendicular to the large-scale cloud.

3.4. Relation between Polarization Segments and the Orientation of Filaments

Figure 5(a) shows the *H*-band polarization segments superposed on the *Spitzer* 8 μm image, together with the location of filaments represented by colored straight lines. In Paper I, these structures were distinguished into hubs and filaments depending on physical features obtained from the NH_3 observations: hubs were classified as structures presenting signs of star formation, as well as higher rotational temperatures and nonthermal velocity dispersions ($T_{\rm rot} \sim 15$ K and $\sigma_{\rm NT} \sim 1\,{\rm km\,s^{-1}}$) than filaments ($T_{\rm rot} \sim 11$ K and $\sigma_{\rm NT} \sim 0.6\,{\rm km\,s^{-1}}$).

Figure 5(b) shows a histogram of the orientation of polarization in the *H* band (θ_H), which includes all the detections shown in Figure 5(a). It clearly exhibits a peak at $\theta_H = 139°$. It is interesting to note that the main orientation at such smaller scales matches very well the average orientation at large scales (from Figure 4).

The relative orientations of segments and filaments are projected onto the plane of the sky, so the true relative orientations are unknown. To carry out a quantitative analysis of the relative orientations, a box was drawn around each filament, with a size matching the length of each structure (from Paper I). Thereafter, segments inside each box were selected in order to represent the orientation of magnetic field lines in the immediate surroundings of each filament. For each vector, its orientation relative to the direction perpendicular to its corresponding filament was computed ($|\theta_H - (\theta_{\rm filament} + 90°)|$).

Figures 5(c) and (d) respectively show the regular distributions and the cumulative distribution functions (CDFs), using the relative orientations of segments for each filament (Hub-S and F60-C2 were omitted). The histograms and CDFs are shown with colored lines that match each respective filament (and its box). Although there is considerable variation in the orientation of polarization segments throughout the field, there is a clear trend for an overall orientation perpendicular to the filaments. This can be seen in the peaks close to zero for some of the histograms in Figure 5(c).

In order to account for the possible effects of geometrical projection, we compared the CDFs to Monte Carlo simulations of a set of relative projected angles based on a large number of vector–filament pairs randomly distributed in three-dimensional space. For each individual simulation, we selected only pairs in which the true relative orientation was within a certain range of values (denoted by Δa). Using this subset of segments, we projected the pairs in the plane of the sky and then computed the CDF of the projected relative orientations. Examples for Δa equal to 0°–20°, 0°–40°, 0°–60°, and 70°–90° are shown in Figure 5(d), as well as the random condition (or 0°–90°).

To find out which Δa configuration from the simulation would best represent the segments' orientations for each filament, we begin by running it for all possible Δa ranges. Then, for each filament, we compare its observed CDF to each of the various simulated CDFs through Kolmogorov–Smirnov tests, which are useful for verifying the statistical probability of two different distributions being drawn from the same ensemble. Finally, the comparison that provided the larger probability was chosen as the best simulation that could represent the observed CDF. Δa for the best representative simulation for each filament is shown in Figure 5(d).

As expected from visual inspection, the majority of the filaments present upper limits on Δa significantly lower than 90°. This means that there is a very clear trend of filaments and hubs being perpendicular to magnetic field lines, even when considering that the orientations of both the filaments and the polarization segments represent a projection on the plane of the sky. There are, however, some situations where the statistics is not ideal (for example, the small number of detections for F10-C and F10-W) and a few exceptions, for example: for Hub-N, the best representative simulation corresponds to a Δa range between 31° and 90°, suggesting a slight trend of magnetic field lines being parallel to the hub. In addition, the distribution for F10-E is only marginally representative of a perpendicular condition. It is interesting to notice that these discrepancies occur exactly for the two structures that are spatially closer to IRAS 18153-1651—the bright ultra-compact H II region to the east of Hub-N and F10-E. This suggests that magnetic field lines in these structures might have been disrupted by the expansion of the H II region. Further discussion is given in Section 4.1.

3.5. Statistical Derivation of the Magnetic Field Strength

In order to understand the interplay between magnetic field support, gravity, and turbulence for each filamentary structure, important physical parameters may be calculated by combining the *H*-band polarization data with velocity dispersion data from molecular-line studies and density information. These parameters are the component of the magnetic field strength in the plane of the sky ($B_{\rm pos}$), the Alfvén Mach number ($M_{\rm A}$), and the ratio of mass to magnetic flux (λ).

Given a set of polarization segments surrounding a certain filament or hub, the Chandrasekhar–Fermi (CF) theory (Chandrasekhar & Fermi 1953) states that the magnetic field strength in that volume of the ISM is inversely proportional to the angular dispersion of polarization segments, a quantity that is related to turbulence. A quantitative method may be applied to study such an angular dispersion factor, which represents the signature of interstellar turbulent motion imprinted in the morphology of magnetic field lines in that area. The method consists in a statistical analysis, proposed first by Hildebrand et al. (2009) and extended later on by Houde et al. (2009), which takes into account the effect of the line-of-sight depolarization. This method has been successfully applied to optical polarization data (Franco et al. 2010) as well as to

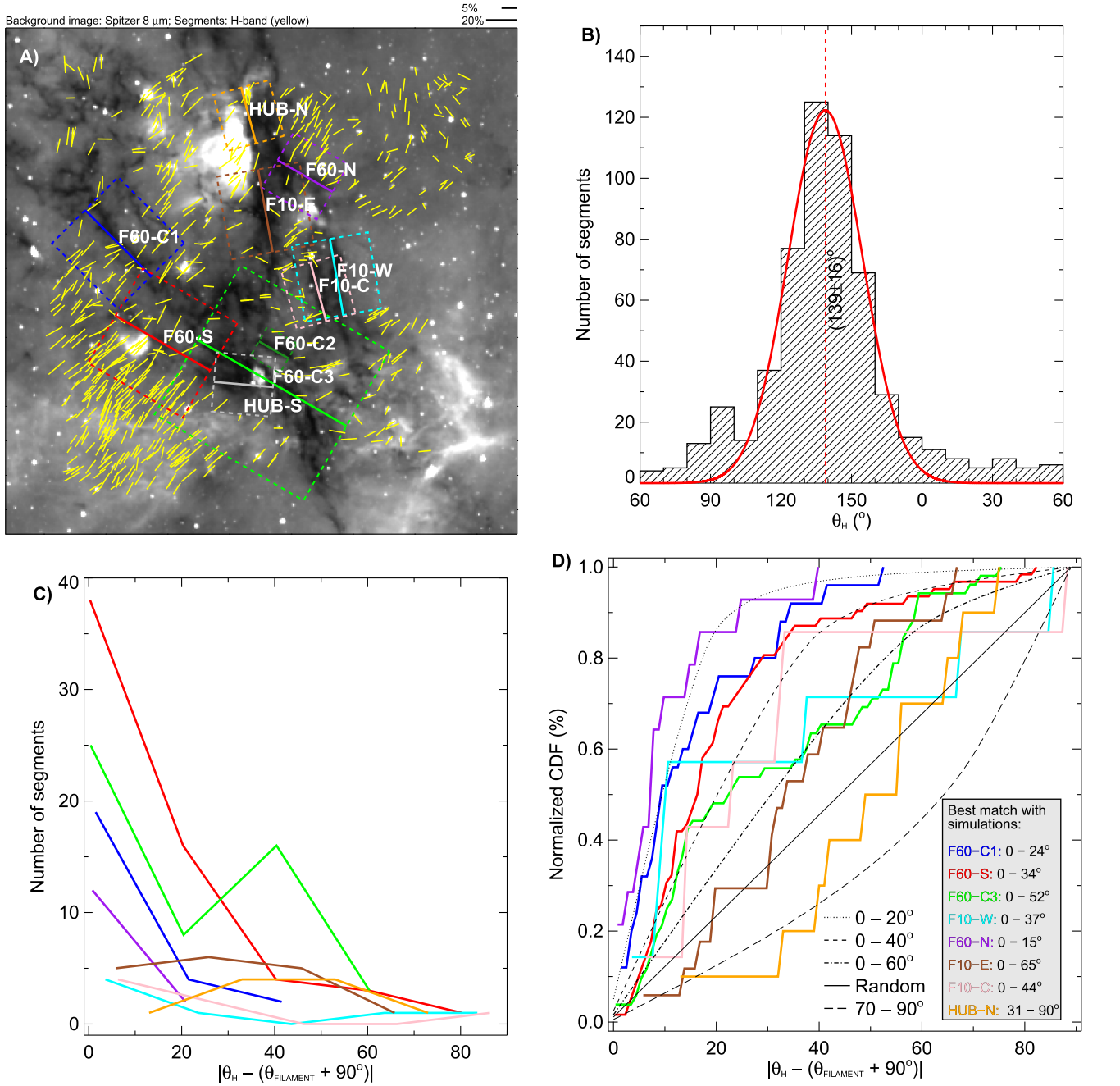

Figure 5. Analysis of the relative orientation between *H*-band polarization segments and interstellar filaments. (a) The *Spitzer* 8 μm image with the polarimetric data (same as Figure 1(d)), as well as dashed colored boxes with sizes equal to each filament's length (represented by the solid lines, as defined in Paper I). (b) The histogram of the orientation of polarization for all *H*-band detections in the field. (c) and (d) The regular histograms and cumulative distribution functions (CDFs), respectively, of the difference between polarization angle and the orientation perpendicular to each filament, considering only the segments within the boxes (the colors match each box in panel (a)). Black lines shows numerical predictions for the CDFs, based on Monte Carlo simulations. Preferential ranges for three-dimensional angle differences of $\Delta a = 0°$–$20°$, $0°$–$40°$, $0°$–$60°$, and $70°$–$90°$ are indicated for reference, as well as a completely random distribution (the solid line). The best match of Δa with the simulations for each filament is listed in the gray box.

submillimeter polarization data (e.g., Houde et al. 2011; Girart et al. 2013; Frau et al. 2014).

As shown by Houde et al. (2009) the angular dispersion function (ADF) can be used to estimate the importance of the magnetic field. We have estimated the ADF, $1 - \langle \cos[\Delta\Phi(l)]\rangle$, where $\Delta\Phi(l)$ is the difference in polarization angles between two points in the plane of the sky separated by a distance l. The analysis is based on the assumption of a stationary, homogenous, and isotropic magnetic field strength and a turbulent correlation length of the magnetic field, δ, smaller than the thickness of the cloud, Δ'. Under these assumptions, the ADF (Equation (42) from Houde et al. 2009) can be expressed as

$$1 - \langle \cos[\Delta\Phi(l)]\rangle \simeq \frac{\langle B_t^2\rangle}{\langle B_0^2\rangle}\frac{1}{N}[1 - e^{l^2/2(\delta^2+2W^2)}] + \sum_{j=1}^{\infty} a'_{2j} l^{2j}, \quad (1)$$

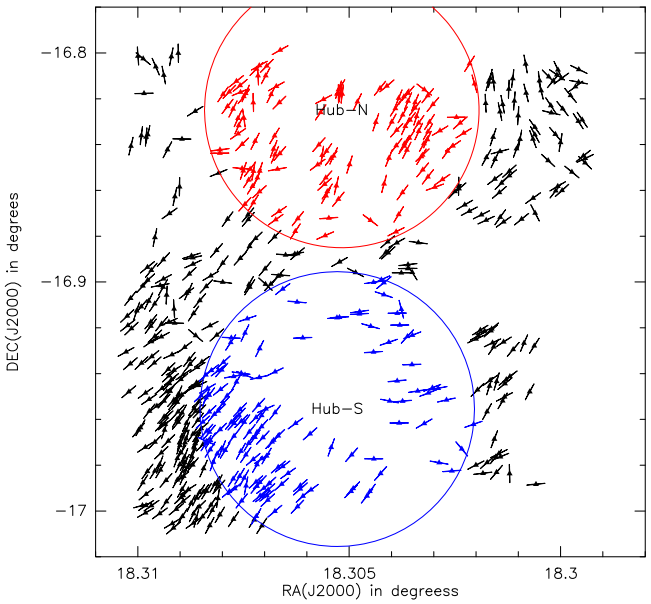

Figure 6. Magnetic field direction obtained from *H*-band polarization data in IRDC G14.2. Red and blue segments indicate the polarization data used to compute the angular dispersion function around Hub-N and Hub-S, respectively.

where l is the length scale, W is the standard deviation of the Gaussian beam ($W = \mathrm{FWHM}/\sqrt{8\ln 2}$), δ is the turbulent correlation length, and N is the number of independent turbulent cells along the line of sight,

$$N = \left[\frac{(\delta^2 + 2W^2)\Delta'}{\sqrt{2\pi}\,\delta^3}\right]. \quad (2)$$

The summation term represents the contribution from the ordered component of the magnetic field that does not involve turbulence. The coefficient a_{2j} represents to the steepness of the function in this ordered component. For stellar polarimetry data, the beam size can be considered as a pencil beam, since W is negligible relative to the turbulent length scale δ (thus W may be ignored). The intercept of the fit to the data of the uncorrelated part at $l = 0$, $f_{\mathrm{NC}}(0)$, allows us to estimate the ratio of turbulent to large-scale magnetic field energy ($\langle B_t^2\rangle/\langle B_0^2\rangle$) as

$$\frac{\langle B_t^2\rangle}{\langle B_0^2\rangle} = N f_{\mathrm{NC}}(0). \quad (3)$$

The low statistics obtained in IRDC G14.2 prevent us from conducting a statistical analysis to fit the ADF for each filament and hub individually. Instead, to analyze the magnetic field, we considered three different regions: the whole cloud, and the two hub–filament systems identified in Paper I, Hub-N and Hub-S. We defined a radius, $R = 0.^{\circ}06$ or ∼2 pc, from the center of each hub (Busquet et al. 2013, 2016) to estimate the ADF for all the measurements that are at a distance $<R$ from the hub. Figure 6 shows the circles centered in each hub for this radius, indicating the polarization values used to compute the ADF for Hub-N (in red) and Hub-S (in blue). The radius of $0.^{\circ}06$ was chosen using the following criteria: (1) to make sure sufficiently wide areas around Hub-N and Hub-S were covered, while also avoiding an overlap between them; (2) to avoid including in the Hub-N area a group of polarization segments

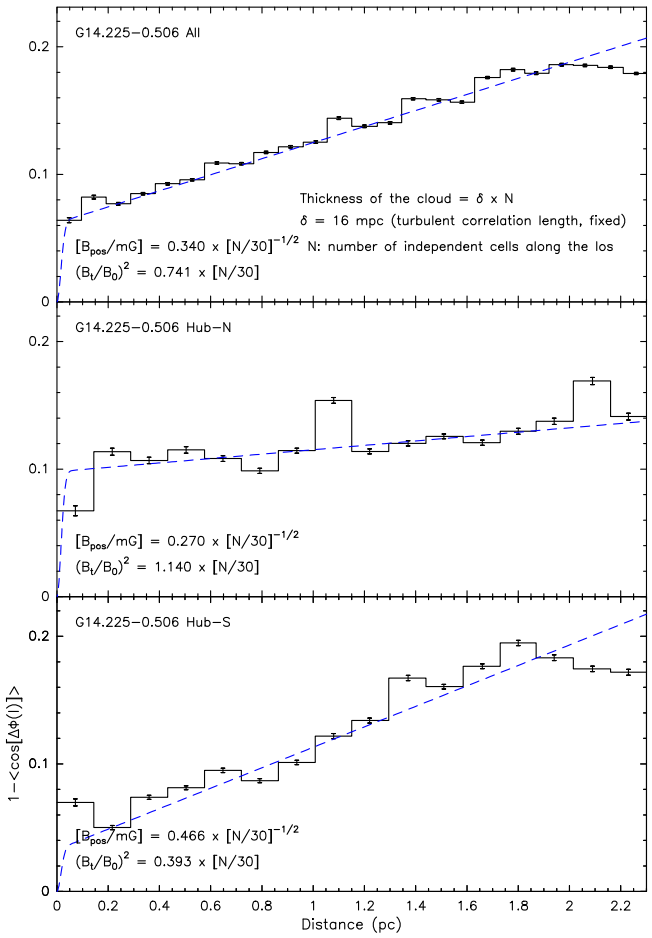

Figure 7. Angular dispersion function of the magnetic field segments detected toward IRDC G14.2 considering all *B*-field segments (top), Hub-N (middle), and Hub-S (bottom). For Hub-N and Hub-S we consider, respectively, the red and blue *B*-field segments shown in Figure 6. The data points and error bars are the mean and standard deviation of all the pairs contained in each bin. The blue dashed line shows the best fit to the data (Equation (1)).

to the right of the red circle that clearly show a different mean orientation, probably related to the edge of RCW 157 (compare with Figures 1(a) and (b)). In Figure 7 we present the ADF for the whole cloud (top panel), Hub-N (middle panel), and Hub-S (bottom panel). One may notice that each function consists of a gradual rise starting from $l = 0$, which may be interpreted as a decrease in the correlation of the orientation of polarization for segments separated by increasingly larger angular distances. The behavior of the ADF is slightly different in the two regions defined around each hub, with Hub-N having a more flattened slope than Hub-S, indicating that the large-scale magnetic field in the plane of the sky is quite uniform. The best fit of Equation (1) to the polarimetric data is shown in Figure 7 by the blue dashed line.

To calculate $\langle B_t^2\rangle/\langle B_0^2\rangle$, we begin by estimating N, which is related to the cloud thickness along the line of sight, $\Delta' = \sqrt{2\pi}\,N\delta$ (see Equation (2)). In other star-forming regions, the turbulent correlation length δ was found to be equal to 16 mpc (OMC-1, Houde et al. 2009; DR21-OH, Girart et al. 2013), or varying between 13 and 33 mpc in NGC 7538 IRS1 (Frau et al. 2014). Based on these previous estimates, in this work we fix $\delta = 16$ mpc since it is not the main source of uncertainty, as will be noted below.

Table 1
Physical Properties in IRDC G14.2

Region	$\langle B_t^2\rangle/\langle B_0^2\rangle$	B_{pos} (mG)	B_{tot} (mG)	M ($M_\odot$)	N_{H_2} (cm^{-2})	λ	M_A
Cloud	0.86 ± 0.62	$0.31^{+0.28}_{-0.07}$	$0.39^{+0.36}_{-0.09}$	4660	2.8×10^{22}	0.6	0.7
Hub-N	1.33 ± 0.95	$0.25^{+0.22}_{-0.06}$	$0.32^{+0.28}_{-0.08}$	2000	4.5×10^{22}	1.1	0.8
Hub-S	0.46 ± 0.33	$0.43^{+0.38}_{-0.10}$	$0.55^{+0.48}_{-0.13}$	1550	3.5×10^{22}	0.5	0.5

Note. Following the method of Houde et al. (2009), the table lists for each defined region the turbulent to uniform magnetic energy ratio, $\langle B_t^2\rangle/\langle B_0^2\rangle$, the magnetic field strength in the plane of the sky, B_{pos}, derived using the CF relation (Equation (4)), the total magnetic field, B_{tot}, the mass, the column density, the ratio of mass to magnetic flux (λ), and the Alfvén Mach number (M_A).

The cloud thickness can be estimated by taking the ratio between the column density N_{H_2} and the volume density $n(H_2)$. We should point out that both quantities are estimated here for the material surrounding the filaments, to coincide with the region where the *H*-band polarization data are distributed. The volume density is the main source of uncertainty for this calculation, so the approach is to find reasonable lower and upper limits around the filaments, and to use this range as a proxy to determine the uncertainty in the magnetic field strength. For the lower limit, we notice that the $C^{18}O$(1–0) line data from IRAM 30 m (G. Busquet et al. 2016, in preparation) reveal an emission present over the entire field of IRDC G14.2, covering not only the dense filaments but also their surroundings. Thus, a conservative estimate for the lower limit is the critical density of $C^{18}O$(1–0), which is $\sim 1.4 \times 10^3\,cm^{-3}$ (Myers 1999). From the same molecular-line survey, we find that the HCN(1–0) line is also detected in the more diffuse area between filaments, thus its effective excitation density of $4.5 \times 10^3\,cm^{-3}$ (assuming a temperature of 20 K, see Table 1 of Shirley 2015) is representative of the typical density in this material. For the upper limit, we know that the density cannot be too much higher than $10^4\,cm^{-3}$, because molecular-line transitions with higher excitation densities (such as the HC_3N (10–9) line, with an excitation density of $4.3 \times 10^4\,cm^{-3}$ at 20 K) are found in emission only toward the densest portions of the filaments. Therefore, we adopt the range of $n(H_2)$ between $\sim 1.4 \times 10^3$ and $10^4\,cm^{-3}$, and propagate the uncertainties into the cloud thickness, $\langle B_t^2\rangle/\langle B_0^2\rangle$, and the magnetic field strength.

The column density (N_{H_2}) can be estimated for the interfilament region by two independent methods: (1) using multiwavelength maps of dust emission (from ground-based telescopes—CSO, APEX—and space-based ones—*Herschel*, *Planck*) to carry out a single-component, modified blackbody fit to each pixel of the maps (Y. Lin et al. 2016, in preparation). The derived values for the region sampled by NIR polarization are typically $T \approx 20$ K and $N_{H_2} \approx 10^{22}\,cm^{-2}$; (2) using the RADEX[8] online one-dimensional non-LTE radiative transfer code (van der Tak et al. 2007) to obtain the column density based on the $C^{18}O$(1–0) line. As inputs to the model of line data, we used a linewidth of $\sim 2\,km\,s^{-1}$, temperatures of 20 K, and volume densities in the range from $\sim 1.4 \times 10^3$ to $10^4\,cm^{-3}$. These inputs result in $C^{18}O$ column densities between $2 \times 10^{22}\,cm^{-2}$ and $5 \times 10^{22}\,cm^{-2}$. Assuming the standard $^{16}O/^{18}O$ ratio for the local ISM of 560 (Wilson & Rood 1994), and adopting the standard abundance of CO with respect to H_2 of 10^{-4}, we find H_2 column densities in the range $1–2 \times 10^{22}\,cm^{-2}$. Therefore, N_{H_2} is well constrained by two independent methods to be $\approx 10^{22}\,cm^{-2}$, and we adopt this as a fixed value to obtain the cloud thickness. The range of cloud thickness is between 0.32 and 2.31 pc, yielding a number of independent cells ranging from $N = 10$ to 60. Using an average value of $N = 35$, this implies that $\langle B_t^2\rangle/\langle B_0^2\rangle$ in the whole cloud is 0.86, while the values are 1.33 and 0.46 in Hub-N and Hub-S, respectively (see Table 1, which also shows the uncertainties). Note that around Hub-N there is equipartition between the perturbed (turbulent) and ordered magnetic field energies, whereas around Hub-S uniform magnetic field dominates energetically over turbulence.

Finally, the CF equation can be used to derive the plane-of-sky magnetic field strength for each region (Equation (57) of Houde et al. 2009):

$$\langle B_0^2\rangle^{1/2} \propto \sigma_v\, n(H_2)^{1/2} [\langle B_t^2\rangle/\langle B_0^2\rangle]^{-1/2}, \quad (4)$$

where σ_v is the velocity dispersion and $n(H_2)$ the volume density. The velocity dispersion was obtained from the $C^{18}O$ (1–0) data (G. Busquet et al. 2016, in preparation) that trace the diffuse gas around the dense filaments and hubs, resulting in $\sim 2\,km\,s^{-1}$. It is important to point out that for the CF method, the relevant component of velocity dispersion is the one generated by turbulence in the ISM. For molecular clouds, the thermal velocity dispersions are typically much smaller than the non-thermal velocity dispersions, so it is reasonable to assume that $\sigma_v = \sigma_{v\,(NT)} + \sigma_{v\,(thermal)} \approx \sigma_{v\,(NT)}$. Moreover, the non-thermal component of velocity dispersion can be produced by turbulent motions, gravitational infall, or rotation. Although numerous star-forming regions present signatures of infall even at larger scales (Peretto et al. 2013, 2014; Duarte-Cabral et al. 2014; Henshaw et al. 2014; Liu et al. 2015; Campbell et al. 2016; Wyrowski et al. 2016), it is unclear whether infall would cause a significant effect in the observed linewidths in comparison with turbulence, especially in the diffuse regions around filaments. In this work, we assume that the velocity dispersion derived from the $C^{18}O$(1-0) data is mostly due to turbulent motions, but this is a matter that will require further investigation.

The ordered component of large-scale magnetic field strength in the plane of the sky, $\langle B_0^2\rangle^{1/2}$, for each defined region is listed in Table 1, where the uncertainties are derived from the range of volume densities $n(H_2)$. Considering the entire set of *H*-band polarization data associated with IRDC G14.2, the sky-projected component of magnetic field strength is 0.39 mG, while for Hub-N and Hub-S it is ~0.32 and 0.55 mG, respectively.

It is important to point out that if the total magnetic field B_{tot} has an inclination $\beta \neq 90°$ with respect to the line of sight, then the CF calculation will lead to underestimated values, since what is being measured is only the plane-of-sky component:

[8] http://var.sron.nl/radex/radex.php

$B_{\rm pos} = B_{\rm tot} \sin\beta$. The inclination β is unknown and therefore it is difficult to correct for this effect in a precise way. However, Crutcher et al. (2004) showed that it is possible to account for it at least statistically by integrating over all possible β values. That leads to the following correction, which is being applied here: $B_{\rm tot} = (4/\pi)B_{\rm pos}$. Table 1 lists the values for the total magnetic field computed for each region, with their respective uncertainties.

3.6. Estimates of Ratios of Mass to Magnetic Flux and Alfvén Mach Numbers

To understand whether magnetic fields are strong enough to support clouds against gravitational collapse, it is useful to study the ratio of mass to magnetic flux (M/Φ), which is conveniently calculated relative to a critical value given by $(M/\Phi)_{\rm crit} = 1/2\pi\sqrt{G}$ (Nakano & Nakamura 1978), where G is the gravitational constant and Φ is the magnetic flux. Crutcher et al. (2004) showed that this relative quantity may be expressed as a function of the H_2 column density (N_{H_2}) and the total magnetic field strength:

$$\lambda = \frac{(M/\Phi)}{(M/\Phi)_{\rm crit}} = 7.6 \times 10^{-21}\left(\frac{N_{\rm H_2}}{\rm cm^{-2}}\right)\left(\frac{B_{\rm tot}}{\mu\rm G}\right)^{-1}. \quad (5)$$

It is known that λ can be affected by the geometry of the cloud (Crutcher et al. 2004). However, given the intricate arrangement of filamentary features in the region of IRDC G14.2, we chose not to make any assumptions regarding its morphology.

Furthermore, in order to assess the importance of the interstellar turbulent motion in disturbing the magnetic field lines, we calculate the Alfvén Mach number, which is given by

$$M_{\rm A} = \frac{\sqrt{3}\,\sigma_v}{V_{\rm A}} \quad (6)$$

where $V_{\rm A} = B_{\rm tot}/\sqrt{4\pi\rho}$ is the Alfvén speed. $M_{\rm A}$ can be viewed as a measure of the ratio between the turbulent and magnetic energies (in fact, this ratio is given by $M_{\rm A}^2$), and therefore the sub-alfvénic ($M_{\rm A} < 1$) or super-alfvénic ($M_{\rm A} > 1$) conditions indicate whether magnetic field support against the gravitational collapse is more or less important than turbulence in the ISM. Notice that, similarly to the CF method, we assume that the non-thermal motions are dominated by turbulence.

To obtain the mass and column density of each defined region we integrate the dust continuum emission at 870 μm (Busquet 2010) over the same area where $B_{\rm pos}$ is measured. Notice that this integration also includes the dense structures within the selected areas, since the goal of calculating λ is to evaluate the gravitational stability of the cloud against magnetic field support. In cold and dense clouds such as IRDCs dust grains are supposed to be coagulated and covered by icy mantles (Peretto & Fuller 2009), so we derived the mass by adopting a dust mass opacity coefficient at 870 μm of 1.7 $\rm cm^2\,g^{-1}$, which corresponds to agglomerated grains with thick ice mantles in cores of density $\sim 10^5\,\rm cm^{-3}$ (Ossenkopf & Henning 1994), and assuming that the dust emission at 870 μm is optically thin; we also assumed a gas-to-dust ratio of 100 and a dust temperature of 17 K. The dust temperature has been obtained using the rotational temperature derived from NH_3 data of Paper I and converted to kinetic temperature through the prescription adopted by Tafalla et al. (2004). For the column density, $N(H_2) = M/\mu m_{\rm H} A$, where $\mu = 2.8$ is the molecular weight per hydrogen molecule, $m_{\rm H}$ is the mass of the hydrogen, and A is the area used to derive the mass. The final values of M, $N(H_2)$, λ, and $M_{\rm A}$ are reported in Table 1. As with the magnetic field values, the uncertainties in λ and $M_{\rm A}$ can reach around a factor of 2. Similar values of $M_{\rm A}$ and λ are found by Pillai et al. (2015) toward two massive IRDCs using submillimeter polarization data.

4. DISCUSSION

4.1. Cloud and Filament Formation through Gravitational Collapse Parallel to Magnetic Field Lines

The polarization data from large to small scales in the region of IRDC G14.2 show that not only are magnetic fields tightly perpendicular to the star-forming dense filamentary structures within (with a few exceptions, as discussed below), but also the cloud as a whole (in which the filaments constitute the densest parts at the center) has an elongated morphology perpendicular to the local magnetic field lines. This suggests a scenario in which magnetic fields have played an important role in regulating the gravitational collapse, being dynamically important in shaping elongated ISM structures from size scales of ~30 pc down to ~2 pc.

It is obvious from Figure 4 that there is a large dispersion in the relative orientation between the *R*-band segments and the cloud. This is not surprising, given that there are numerous hierarchical substructures and diffuse filamentary features around the entire region, as shown by the *Herschel* image (Figure 1(c)). Some coupling between the magnetic field lines and these diffuse clouds is expected, which may explain a fraction of the dispersion observed. However, the general trend of magnetic fields perpendicular to the cloud is still evident.

At smaller scales (~2 pc), the analysis on Figure 5 shows that filaments and hubs are remarkably well oriented perpendicularly to magnetic field lines. It is interesting to see that field lines show some smooth variations in orientation inside this area, and the orientations of filaments seem to follow these smooth variations. This is a further indication that magnetic fields favored the gravitational collapse of these structures parallel to field lines.

There are two important exceptions: Hub-N, which exhibits a slight trend of magnetic field lines parallel to the structure; and F10-E, which shows only a marginal perpendicular correlation with the filament axis. It is possible that the original field morphology in this area has been disrupted due to its proximity to IRAS 18153-1651, an ultra-compact H II region seen in the *Spitzer* 8 μm image as a bright extended area right next to Hub-N (Figure 5(a)). Paper I showed that this hub has likely been heated by the interaction with the ultra-compact H II region, and its NH_3 velocity is consistent with an expanding shell. This is consistent with the fact that the ratio of turbulent to uniform magnetic field energy ($\langle B_{\rm t}^2\rangle/\langle B_0^2\rangle$) is higher in Hub-N than in Hub-S and the entire cloud.

Recent observations show that the presence of magnetic fields aligned perpendicularly to filaments seems to be a ubiquitous characteristic of star-forming clouds (e.g., Franco et al. 2010; Li et al. 2013; Zhang et al. 2014), at least when considering densities above a certain threshold. The most recent evidence comes from the all-sky polarimetic observations of the *Planck* space telescope: by analyzing a group of nearby molecular clouds, Planck Collaboration et al. (2016) showed that the relative orientation studied as a function of

column density gradually changes from preferentially parallel or random to preferentially perpendicular. Furthermore, previous works by Goldsmith et al. (2008) and Tassis et al. (2009) also showed that magnetic fields within dense environments are most likely perpendicular to the main filamentary structures, perhaps even being responsible for channeling interstellar material through diffuse striated features that are also perpendicular to the filaments. More recently, Zhang et al. (2014) surveyed a sample of 14 massive star-forming clumps and filaments at 870 μm using the polarimeter on the Submillimeter Array. By comparing the dust polarization at dense core scales of 0.01–0.1 pc with the parsec-scale polarization, they concluded that magnetic fields play an important role in channeling gas during the collapse of the clump and the formation of dense cores. Therefore, magnetic fields appear to be dynamically important even at scales smaller than 1 pc.

Paper I pointed out that, particularly in IRDC G14.2, some striations are seen in the NH_3 map, converging towards filament F10-E. A visual inspection of the *H*-band polarization map shows that segments superposed on the striations are parallel to them, and perpendicular to the main filament, suggesting that flows of material possibly converging into the main filament are parallel to magnetic fields (red arrows in Figures 1(b) and (d)). Some striations parallel to polarization segments may also be seen after a close visual inspection of the Hα image (Figure 1(b), red arrows along its bottom-left portion), which are identified as dark patches observed against a bright extended emission. This suggests a scenario similar to those observed in the Taurus molecular cloud (Goldsmith et al. 2008), in the Riegel–Crutcher cloud (McClure-Griffiths et al. 2006), and in Lupus I (Franco & Alves 2015). However, in these three examples, the interstellar structures were nearby, which allowed a clearer view of the diffuse striations.

It is instructive to point out that an alternative explanation for the perpendicular condition between filaments and magnetic field lines could be proposed: the same configuration would be expected if magnetic field lines were dragged inwards by infalling material, which could also produce the striations previously mentioned. However, it is difficult to reconcile this scenario with the fact that magnetic fields at large scales are also perpendicular to the filamentary features inside the cloud. In addition, the magnetically dominated gravitational collapse scenario is supported by MHD simulations, as described in Section 4.2.

4.2. Comparison with Simulations and Analysis of Stability against Magnetic Field Support and Turbulent Motions

Recently, Van Loo et al. (2014) developed numerical simulations designed to model the nonlinear evolution of a gravitational instability within a layer of interstellar material threaded by magnetic fields. The simulations show that although the presence of magnetic fields does not seem to influence the filaments' central density profiles (which are more consistent with a typical hydrodynamic equilibrium structure), they play an important role in determining their morphological and spatial distribution. While weak magnetic fields lead to filamentary features like a spider's web, strong magnetic fields often generate a network of parallel filaments aligned perpendicular to field lines.

Given the similarities of the model outcomes to the morphological features of IRDC G14.2, Van Loo et al. (2014) compared their simulations with a fraction of the area of IRDC G14.2 (specifically around Hub-N) using the polarimetric data from this work that were available at that time in Paper I. They find that the formation of these filaments is consistent with fragmentations of a layer threaded with strong magnetic fields, leading to parallel elongated structures perpendicular to field lines. The polarimetric observations from the present work provide further support for this model, and generalize its conclusions for the entire filamentary network of IRDC G14.2. The high magnetic field strengths estimated here ($\approx$320–550 μG) support a scenario in which the initial conditions favored a collapse of density perturbations parallel to magnetic fields, leading to the morphology of parallel filaments currently observed. Van Loo et al. (2014) estimated that the magnetic field values for IRDC G14.2 would need to be stronger than 12–25 μG in their "strong magnetic field" model, in which parallel filaments are expected to be formed. Our estimated values are one order of magnitude higher than this lower limit, showing that IRDC G14.2 is well into the strong magnetic field regime.

Alfvén Mach numbers (M_A) calculated for each defined region show that the sub-alfvénic condition is pervasive at these small scales, implying that the magnetic field strength dominates over the turbulent motion. Furthermore, the values of λ are in the range 0.5–1.1, suggesting a sub-critical condition (although they are close to the critical value, especially considering that there is an uncertainty in the cloud's thickness). However, active star formation is already taking place (Wang et al. 2006; Povich & Whitney 2010), suggesting that although magnetic fields seem to be strong enough to dominate over turbulence, this was usually not sufficient to prevent the gravitational collapse, which eventually led to star formation. Therefore the close-to-critical condition might be related to the filaments' envelopes, while the denser interior (not probed by the polarization data) has probably reached supercritical conditions. λ values may depend on whether the envelopes or the cores are probed (Bertram et al. 2012).

4.3. Magnetic Fields Related to the Evolutionary Sequence of the IRDC G14.2 Complex

Using single-dish ^{12}CO observations, Elmegreen & Lada (1976) provided the first description of the molecular cloud in which IRDC G14.2 is located, dividing the region into four fragments named A–D. Fragment C is roughly coincident with the position of IRDC G14.2. According to Elmegreen & Lada (1976), these fragments seem to be part of an evolutionary sequence: nearby star-forming region M17, together with fragments A and B, is somewhat more evolved, while fragments C and D appear to be younger.

Using the densities and velocity dispersions from the ^{12}CO data, Elmegreen & Lada (1976) estimated that the fragments appear to be contracting on a timescale that is 2–3 times longer than the free-fall time, suggesting that strong internal magnetic fields of $\sim$340 μG could be providing some support against the collapse in fragment C. Their estimate, which is based on equipartition, is remarkably similar to the values of magnetic field strengths computed in this work for the filamentary structures within IRDC G14.2. However, it is important to point out that interstellar structures with larger aspect ratios (such as filamentary features) have longer collapse timescales than spherical clouds (Pon et al. 2012). Thus, an alternative

explanation for the discrepancy in contraction time by a factor of 2–3 observed by Elmegreen & Lada (1976) is due to the filamentary nature of the cloud, which could not be inferred using the low-resolution ^{12}CO data.

Another interesting evolutionary aspect of this region, revealed by Povich & Whitney (2010), is that there seems to be a lack of O-type stars, leading to an initial mass function significantly steeper than the Salpeter one. It is unclear, however, whether the support against gravitational collapse provided by strong magnetic fields had any influence on halting or delaying the formation of massive stars.

4.4. Magnetic Fields in the H II Region RCW 157

In mapping the large-scale interstellar polarization around IRDC G14.2, a significant fraction of the H II region RCW 157 was covered (top right of Figures 1(a) and (c)). Therefore, as a side-product of this work, it offers the opportunity to analyze the magnetic field morphology in this structure, at least in a qualitative manner. Figure 1(a) shows that this area is dominated by a bright Hα extended emission. Pillars and "elephant trunks" are seen as dark patches in absorption against this bright Hα glow, extending inwards at the edge of the H II region (black arrow in Figure 1(a)). These finger-shaped features are usually generated by radiatively driven effects, and are commonly observed in this kind of environment.

It is clear that the general orientation of polarization towards RCW 157 is markedly different from that in the southern areas (compare Figure 1(c) above and below the dashed yellow line): the segments usually span orientations between 80° and 100°, while the typical large-scale orientation in the area of IRDC G14.2 is ≈140°. Moreover, although several interstellar substructures are observed at RCW 157, the magnetic field morphology seems fairly well oriented: in particular, in the northern portion of the map ($\alpha < 18^{\rm h}17^{\rm m}30^{\rm s}$ and $\delta > -16°38'$), the angular dispersion is only 15°. Furthermore, along the edges of the H II region, polarization segments in general are parallel to the borders (i.e., parallel to the dashed yellow line). In previous works, it has been shown that the expansion of an H II region can modify the original magnetic field orientation, piling up field lines along its borders (Santos et al. 2012, 2014). The higher magnetic field strength due to the piling effect can lead to low dispersions of polarization angle. These qualitative features observed at RCW 157 suggest that a similar effect might be ongoing in this area. The uniformly oriented polarization segments are probably probing the expanding interstellar shell along the line of sight.

It is also interesting to see that the finger-shaped pillars are parallel to polarization segments. This configuration is expected, because during the formation of these structures, magnetic fields are swept out by the expanding front and its lines are wrapped around the pillars. These observations give support to radiation–MHD simulations of H II regions forming within magnetized molecular clouds, which predict very similar characteristics (Arthur et al. 2011; Peters et al. 2011).

5. CONCLUSIONS

In this work we have studied the morphological relation between magnetic fields and the various interstellar structures in the star-forming complex IRDC G14.2. Our goal was achieved through polarimetric observations of background stars in the optical and NIR spectral bands, aimed respectively at the large-scale cloud and the small-scale filamentary structures within its densest portions. The analysis was carried out after careful removal and correction of the foreground polarization component. Below is a list of the main conclusions.

1. We compared the orientation of magnetic fields with filaments and hubs, and also with the molecular cloud in which these structures are embedded. It is clear that magnetic fields are perpendicular both to the small-scale filamentary features and to the large-scale cloud. For filaments, this condition holds true with few exceptions, even when considering Monte Carlo simulations that account for sky-projection effects. These characteristics are consistent with a scenario in which magnetic fields regulated the gravitational collapse from large (≈30 pc) to small (≈2 pc) scales.
2. Combining the polarization data with observations of dust emission and molecular lines, we estimate total magnetic field strengths, Alfvén Mach numbers, and ratios of mass to magnetic flux. The structures are predominantly in a sub-alfvénic and close-to-critical condition, suggesting that magnetic fields are strong enough to overcome turbulent motions, but not sufficient to prevent the gravitational collapse. The high magnetic field values corroborate previous numerical simulations that show that these conditions eventually lead to a gravitational instability developing along magnetic field lines, therefore generating filaments organized in a parallel arrangement.
3. The range of magnetic field values obtained for the filaments and hubs (≈320–550 μG) is consistent with estimates based on simple assumptions of equipartition by Elmegreen & Lada (1976), who suggested that internal magnetic field strengths would be around 340 μG. According to their interpretation, the presence of such strong magnetic fields might be a necessary condition to explain why the large-scale cloud is possibly contracting on a timescale 2–3 times longer than what is expected from the free-fall time.

As a precursor to a massive OB association presenting numerous filamentary interstellar features and young stellar sources, the cloud IRDC G14.2 proves to be an ideal star-forming site in which to study the underlying physical conditions regulating the gravitational collapse. This is an important target for additional analysis, particularly using high-resolution surveys of polarized emission (in the far-infrared or submillimeter wavelengths) or even spectral data focused on Zeeman splitting. This would be a natural continuation of this work, given the significant role played by magnetic fields in shaping the filamentary morphology and regulating the collapse. More specifically, magnetic field strengths (along with $M_{\rm A}$ and λ values) could be better constrained with this kind of observation, especially if comparisons with numerical simulations are made, assuming the specific physical conditions of this cloud and its substructures.

We are grateful to the anonymous referee for valuable suggestions and comments. We thank the staff of OPD/LNA (Brazil) for their hospitality and invaluable help during our observing runs. G.A.P.F. and F.P.S. acknowledge support from the Brazilian agencies CNPq, CAPES, and FAPEMIG. F.P.S. was supported by the CAPES grant 2397/13-7. G.B.

acknowledges the support from the Spanish Ministerio de Economia y Competitividad (MINECO) under grant FPDI-2013-18204. G.B. and J.M.G. are supported by the Spanish MICINN grant AYA2011-30228-C03 and the MINECO grant AYA2014-57369-C3. This investigation made extensive use of data products from the Two Micron All Sky Survey (2MASS), which is a joint project of the University of Massachusetts and the Infrared Processing and Analysis Center/California Institute of Technology, funded by the National Aeronautics and Space Administration and the National Science Foundation. This research is based in part on observations made with the *Spitzer* Space Telescope, which is operated by the Jet Propulsion Laboratory, California Institute of Technology under a contract with NASA. We are grateful to Drs. A. M. Magalhães and A. Pereyra for providing the polarimetric unit and the software used for data reductions.

Facility: LNA:1.6 m.

REFERENCES

Alves, F. O., Franco, G. A. P., & Girart, J. M. 2008, A&A, 486, L13
Alves, F. O., Frau, P., Girart, J. M., et al. 2014, A&A, 569, L1
Anderson, L. D., Zavagno, A., Deharveng, L., et al. 2012, A&A, 542, A10
Andersson, B.-G., Pintado, O., Potter, S. B., Straižys, V., & Charcos-Llorens, M. 2011, A&A, 534, A19
André, P., Men'shchikov, A., Bontemps, S., et al. 2010, A&A, 518, L102
Anglada, G., Estalella, R., Pastor, J., Rodriguez, L. F., & Haschick, A. D. 1996, ApJ, 463, 205
Arthur, S. J., Henney, W. J., Mellema, G., de Colle, F., & Vázquez-Semadeni, E. 2011, MNRAS, 414, 1747
Arzoumanian, D., André, P., Didelon, P., et al. 2011, A&A, 529, L6
Avedisova, V. S., & Palous, J. 1989, BAICz, 40, 42
Benjamin, R. A., Churchwell, E., Babler, B. L., et al. 2003, PASP, 115, 953
Bertram, E., Federrath, C., Banerjee, R., & Klessen, R. S. 2012, MNRAS, 420, 3163
Bronfman, L., Nyman, L.-A., & May, J. 1996, A&AS, 115, 81
Busquet, G. 2010, PhD thesis, Univ. Barcelona
Busquet, G., Estalella, R., Palau, A., et al. 2016, ApJ, 819, 139
Busquet, G., Zhang, Q., Palau, A., et al. 2013, ApJL, 764, L26
Campbell, J. L., Friesen, R. K., Martin, P. G., et al. 2016, ApJ, 819, 143
Carey, S. J., Noriega-Crespo, A., Mizuno, D. R., et al. 2009, PASP, 121, 76
Carpenter, J. M. 2001, AJ, 121, 2851
Chandrasekhar, S., & Fermi, E. 1953, ApJ, 118, 113
Clemens, D. P., & Tapia, S. 1990, PASP, 102, 179
Crutcher, R. M., Nutter, D. J., Ward-Thompson, D., & Kirk, J. M. 2004, ApJ, 600, 279
Deharveng, L., Schuller, F., Anderson, L. D., et al. 2010, A&A, 523, A6
Dobashi, K., Marshall, D. J., Shimoikura, T., & Bernard, J.-P. 2013, PASJ, 65, 31
Dolginov, A. Z., & Silantev, N. A. 1976, Ap&SS, 43, 337
Draine, B. T., & Weingartner, J. C. 1996, ApJ, 470, 551
Duarte-Cabral, A., Bontemps, S., Motte, F., et al. 2014, A&A, 570, A1
Elmegreen, B. G., & Lada, C. J. 1976, AJ, 81, 1089
Fissel, L. M., Ade, P. A. R., Angilè, F. E., et al. 2016, ApJ, 824, 134
Fitzpatrick, E. L. 1999, PASP, 111, 63
Franco, G. A. P., & Alves, F. O. 2015, ApJ, 807, 5
Franco, G. A. P., Alves, F. O., & Girart, J. M. 2010, ApJ, 723, 146
Frau, P., Girart, J. M., Zhang, Q., & Rao, R. 2014, A&A, 567, A116
Girart, J. M., Beltrán, M. T., Zhang, Q., Rao, R., & Estalella, R. 2009, Sci, 324, 1408
Girart, J. M., Frau, P., Zhang, Q., et al. 2013, ApJ, 772, 69
Girart, J. M., Rao, R., & Marrone, D. P. 2006, Sci, 313, 812
Goldsmith, P. F., Heyer, M., Narayanan, G., et al. 2008, ApJ, 680, 428
Gómez, G. C., & Vázquez-Semadeni, E. 2014, ApJ, 791, 124
Gomez, H. L., Krause, O., Barlow, M. J., et al. 2012, ApJ, 760, 96
Heiles, C. 2000, AJ, 119, 923
Heiles, C., & Crutcher, R. 2005, in Lecture Notes in Physics Vol. 664, Cosmic Magnetic Fields, ed. R. Wielebinski & R. Beck (Berlin: Springer), 137
Henshaw, J. D., Caselli, P., Fontani, F., Jiménez-Serra, I., & Tan, J. C. 2014, MNRAS, 440, 2860
Hildebrand, R. H., Kirby, L., Dotson, J. L., Houde, M., & Vaillancourt, J. E. 2009, ApJ, 696, 567
Hill, T., Motte, F., Didelon, P., et al. 2011, A&A, 533, A94
Houde, M., Rao, R., Vaillancourt, J. E., & Hildebrand, R. H. 2011, ApJ, 733, 109
Houde, M., Vaillancourt, J. E., Hildebrand, R. H., Chitsazzadeh, S., & Kirby, L. 2009, ApJ, 706, 1504
Jaffe, D. T., Guesten, R., & Downes, D. 1981, ApJ, 250, 621
Jaffe, D. T., Stier, M. T., & Fazio, G. G. 1982, ApJ, 252, 601
Jiménez-Serra, I., Caselli, P., Tan, J. C., et al. 2010, MNRAS, 406, 187
Jones, T. J., Bagley, M., Krejny, M., Andersson, B.-G., & Bastien, P. 2015, AJ, 149, 31
Koornneef, J. 1983, A&A, 128, 84
Larson, K. A., Whittet, D. C. B., & Hough, J. H. 1996, ApJ, 472, 755
Lazarian, A. 2007, JQSRT, 106, 225
Li, H.-b., Fang, M., Henning, T., & Kainulainen, J. 2013, MNRAS, 436, 3707
Li, H.-B., Yuen, K. H., Otto, F., et al. 2015, Natur, 520, 518
Lis, D. C., Serabyn, E., Keene, J., et al. 1998, ApJ, 509, 299
Liu, H. B., Galván-Madrid, R., Jiménez-Serra, I., et al. 2015, ApJ, 804, 37
Lockman, F. J. 1989, ApJS, 71, 469
Magalhaes, A. M., Rodrigues, C. V., Margoniner, V. E., Pereyra, A., & Heathcote, S. 1996, in ASP Conf. Ser. 97, Polarimetry of the Interstellar Medium, ed. W. G. Roberge & D. C. B. Whittet (San Francisco, CA: ASP), 118
Mathewson, D. S., & Ford, V. L. 1970, MmRAS, 74, 139
McClure-Griffiths, N. M., Dickey, J. M., Gaensler, B. M., Green, A. J., & Haverkorn, M. 2006, ApJ, 652, 1339
Minier, V., Tremblin, P., Hill, T., et al. 2013, A&A, 550, A50
Molinari, S., Swinyard, B., Bally, J., et al. 2010, A&A, 518, L100
Myers, P. C. 1999, in NATO Advanced Science Institutes (ASI) Ser. C, Proc. 540, The Origin of Stars and Planetary Systems, ed. C. J. Lada & N. D. Kylafis (Dordrecht: Kluwer), 67
Myers, P. C. 2009, ApJ, 700, 1609
Nagai, T., Inutsuka, S.-i., & Miyama, S. M. 1998, ApJ, 506, 306
Nakajima, Y., & Hanawa, T. 1996, ApJ, 467, 321
Nakamura, F., & Li, Z.-Y. 2008, ApJ, 687, 354
Nakamura, F., Miura, T., Kitamura, Y., et al. 2012, ApJ, 746, 25
Nakano, T., & Nakamura, T. 1978, PASJ, 30, 671
Ossenkopf, V., & Henning, T. 1994, A&A, 291, 943
Palagi, F., Cesaroni, R., Comoretto, G., Felli, M., & Natale, V. 1993, A&AS, 101, 153
Parker, Q. A., Phillipps, S., Pierce, M. J., et al. 2005, MNRAS, 362, 689
Penprase, B. E., Lauer, J., Aufrecht, J., & Welsh, B. Y. 1998, ApJ, 492, 617
Peretto, N., & Fuller, G. A. 2009, A&A, 505, 405
Peretto, N., Fuller, G. A., André, P., et al. 2014, A&A, 561, A83
Peretto, N., Fuller, G. A., Duarte-Cabral, A., et al. 2013, A&A, 555, A112
Pereyra, A. 2000, PhD thesis, Univ. São Paulo
Peters, T., Banerjee, R., Klessen, R. S., & Mac Low, M.-M. 2011, ApJ, 729, 72
Pilbratt, G. L., Riedinger, J. R., Passvogel, T., et al. 2010, A&A, 518, L1
Pillai, T., Kauffmann, J., Tan, J. C., et al. 2015, ApJ, 799, 74
Planck Collaboration, Ade, P. A. R., Aghanim, N., et al. 2015, A&A, 576, A104
Planck Collaboration, Ade, P. A. R., Aghanim, N., et al. 2016, A&A, 586, A138
Plume, R., Jaffe, D. T., & Evans, N. J., II 1992, ApJS, 78, 505
Pon, A., Toalá, J. A., Johnstone, D., et al. 2012, ApJ, 756, 145
Povich, M. S., & Whitney, B. A. 2010, ApJL, 714, L285
Reis, W., Corradi, W., de Avillez, M. A., & Santos, F. P. 2011, ApJ, 734, 8
Reiz, A., & Franco, G. A. P. 1998, A&AS, 130, 133
Santos, F. P., Corradi, W., & Reis, W. 2011, ApJ, 728, 104
Santos, F. P., Franco, G. A. P., Roman-Lopes, A., Reis, W., & Román-Zúñiga, C. G 2014, ApJ, 783, 1
Santos, F. P., Roman-Lopes, A., & Franco, G. A. P. 2012, ApJ, 751, 138
Schneider, N., Csengeri, T., Bontemps, S., et al. 2010, A&A, 520, A49
Serkowski, K., Mathewson, D. L., & Ford, V. L. 1975, ApJ, 196, 261
Shirley, Y. L. 2015, PASP, 127, 299
Skrutskie, M. F., Cutri, R. M., Stiening, R., et al. 2006, AJ, 131, 1163
Tafalla, M., Myers, P. C., Caselli, P., & Walmsley, C. M. 2004, A&A, 416, 191
Tassis, K., Dowell, C. D., Hildebrand, R. H., Kirby, L., & Vaillancourt, J. E. 2009, MNRAS, 399, 1681
Tody, D. 1986, Proc. SPIE, 627, 733
Turnshek, D. A., Bohlin, R. C., Williamson, R. L., et al. 1990, AJ, 99, 1243
van der Tak, F. F. S., Black, J. H., Schöier, F. L., Jansen, D. J., & van Dishoeck, E. F. 2007, A&A, 468, 627
Van Loo, S., Keto, E., & Zhang, Q. 2014, ApJ, 789, 37

Wang, Y., Zhang, Q., Rathborne, J. M., Jackson, J., & Wu, Y. 2006, ApJL, 651, L125
Wardle, J. F. C., & Kronberg, P. P. 1974, ApJ, 194, 249
Whittet, D. C. B., Hough, J. H., Lazarian, A., & Hoang, T. 2008, ApJ, 674, 304
Wilking, B. A., Lebofsky, M. J., Kemp, J. C., Martin, P. G., & Rieke, G. H. 1980, ApJ, 235, 905
Wilking, B. A., Lebofsky, M. J., & Rieke, G. H. 1982, AJ, 87, 695
Wilson, T. L., & Rood, R. 1994, ARA&A, 32, 191
Wu, Y. W., Sato, M., Reid, M. J., et al. 2014, A&A, 566, A17
Wyrowski, F., Güsten, R., Menten, K. M., et al. 2016, A&A, 585, A149
Xu, Y., Moscadelli, L., Reid, M. J., et al. 2011, ApJ, 733, 25
Zhang, Q., Qiu, K., Girart, J. M., et al. 2014, ApJ, 792, 116